applied sciences

MDPI

Article

Enhanced Modeling for Analysis of Fine Particulate Interactions with Coated Surfaces

Hao Wu and Meng Liu *

School of Aeronautic Science and Engineering, Beihang University, Beijing 100191, China; haowu@buaa.edu.cn
* Correspondence: liumeng@buaa.edu.cn

Abstract: The adhesion of Martian surface dust to solar panels has been a longstanding challenge for Mars mission researchers. Anti-dust coatings have been developed to deter the adsorption of dust particles onto these solar panels. However, current ground testing methods struggle to accurately verify and assess the coating's ability to inhibit dust particle adsorption. Consequently, this paper introduces a computational model capable of calculating the contact force between fine particles and the coated surface. This model, grounded in the classical adhesive elastic interactions paradigm, establishes a normal force solution by approximating the pressure distribution on the contact area between the sphere and the coating, subsequently computing the composite force acting on the particle. Utilizing the API module of the EDEM simulation platform, we conducted simulations of the motion of fine particles on both smooth and coated plates. The results reveal that van der Waals forces are more prominent for light-mass particles, and the application of the coating can diminish the pull of these forces, facilitating easier detachment of dust particles from the plate surface.

Keywords: Martian dust; fine particles; particle interactions; discrete element method

check for updates

Citation: Wu, H.; Liu, M. Enhanced Modeling for Analysis of Fine Particulate Interactions with Coated Surfaces. *Appl. Sci.* **2024**, *14*, 1896. https://doi.org/10.3390/app14051896

Academic Editor: Elisa Sani

Received: 5 February 2024
Revised: 14 February 2024
Accepted: 24 February 2024
Published: 25 February 2024

Copyright: © 2024 by the authors. Licensee MDPI, Basel, Switzerland. This article is an open access article distributed under the terms and conditions of the Creative Commons Attribution (CC BY) license (https://creativecommons.org/licenses/by/4.0/).

1. Introduction

Surface dust on Mars has persistently posed a significant challenge to Martian exploration efforts, with observable effects including wear and tear on equipment, adsorption, and electromagnetic interference. The accumulation of fine dust particles on solar panels substantially reduces the energy provision for Mars exploration apparatus, posing a severe threat to the operational lifespan of rovers [1]. Consequently, dust management for Mars rovers remains a pressing priority. This holds true even for the meticulously designed solar panels of NASA's Mars rovers [2,3], as well as China's Zhurong rover [4], all of which have had to contend with Martian dust.

The advent of dust removal technology has become a necessary precursor to Mars exploration. A variety of such technologies have been developed [5], including the wind cleaning method [1], anti-dust coating method [6], mechanical wiping method [7], and electrodynamic screen method [8]. The anti-dust coating method [9] is usually chosen as one of the main dust removal strategies for Mars rovers due to its high reliability. Xu et al. [6] advanced this field by developing nano-crystalline composite coatings that provide effective dust protection for solar panels. By employing an ultra-thin solar film in conjunction with a specialized anti-dust coating, the Zhurong rover managed to achieve dust removal efficiency exceeding 86% [10].

Laboratory testing for dust removal efficiency serves as the primary method of evaluating coatings. Zhang et al. [11] conducted performance tests on coatings with varying hydrolysate-silica sol mass ratios, but did not elaborate on the size distribution of the particles involved. Dogra et al. [12] examined the wetting behavior and transmittance of hydrophobic coatings prepared using zirconium nanoparticles and hexamethyldisilazane (HMDS). However, investigations into these coatings' effectiveness in removing specific dust types from the Martian surface remain unexplored. Conducting laboratory research

on the effectiveness of anti-dust coatings for Martian dust removal poses considerable challenges. Replicating the exact environment of the Martian surface within a lab setting is not only costly; the accuracy of simulating certain environmental parameters (e.g., gravitational conditions) also remains questionable. Furthermore, while dust removal tests on coatings have shown promising results with larger particles (e.g., those measuring millimeters in diameter [9]), their effectiveness on finer particles, particularly those with diameters in the tens of micrometers range, is yet to be definitively established. Perko et al. [13] compiled insights from various research studies on Martian surface dust. As gleaned from the literature, dust particles typically found on surfaces are usually smaller than 100 µm. Fine particles with sizes ranging from 5 µm to 100 µm can be swept up during dust storms, while particles smaller than 10 µm might potentially remain suspended indefinitely within the Martian atmosphere. In the force analysis of such fine particles, van der Waals forces should not be overlooked as they may play a significant role in causing fine particles to adhere to surfaces [14]. Nevertheless, carrying out dust removal tests for these fine particles presents numerous challenges. Accurate measurement and observation stand as primary difficulties, while accurately simulating the environmental conditions and the behavior of fine particles poses another formidable hurdle.

The discrete element method (DEM) [15] is an increasingly prominent particle simulation approach suitable for studies that are challenging to conduct within a laboratory setting. This technique breaks down the research object (be it particle or geometric) into independent units, conducts an analysis of interactions among these units, and proceeds to iteratively calculate force and displacement at each time step based on Newton's laws of motion. EDEM, notably the first modeling and simulation software developed using the DEM [16], has proven successful in various fields. Examples of its application include characterizing material movement in loader shovels [17], analyzing particle trajectories in mixers [18], and understanding the crushing process of gold-bearing ore in a jaw crusher [19]. The built-in JKR model [20] within EDEM is a cohesive contact model, taking into account the influence of van der Waals forces within the contact zone. This allows users to simulate highly adhesive systems. However, this model struggles to accurately capture the dynamics of fine particles interacting with the coating surface. One reason for this is the disparity in scale—several orders of magnitude—between the surface resolution of the coating and the size of the particles, which complicates geometry design. Additionally, EDEM^{TM} 2022.1 software identifies contact based solely on coordinate distance [21], disregarding the surface properties of the coating. Therefore, accurately characterizing the force interactions between fine particles and coatings is crucial for analyzing the dust removal capabilities of these coatings and conducting dynamic simulations of fine particles.

Drawing from the Hertz contact theory that offers a comprehensive analysis and derivation of elastic contact, this study aims to conduct an analysis of interactions between fine particles and coating surfaces. The central purpose is to develop a computational model that can accurately portray the contact between particles and coatings. Through an in-depth analysis of the coating's structural intricacies, we construct a simplified equation for estimating the pressure distribution at the interface between the particle and the coating surface. Consequently, this allows us to deduce the normal force acting upon the particle at the coating surface. The model introduced in this study, synergizing with the dynamic simulation capacities of EDEM software, serves as an efficient simulation tool for prospective dust removal tests for coatings. Moreover, it lays a foundation for simulating and evaluating surface dust removal capabilities of future Mars rovers.

This paper is organized as follows. In Section 2, the theoretical model is provided. Numerical simulations and discussions are carried out in Section 3. Section 4 draws the conclusions.

2. Theoretical Model

This paper primarily investigates fine particles, smaller than 100 microns, adhering to solar panel surfaces. To facilitate a comprehensive analysis of force characteristics related to

particulate matter, we used an idealized uniform sphere as a representative physical model. Considering the thin atmospheric conditions on Mars, for fine particles, the Knudsen number—pertaining to the airflow circulating around these particles—generally exceeds 0.01. This suggests that the interaction pattern between the airflow and these microscopic entities is largely discontinuous [22]. Additionally, our study primarily focuses on the adsorption characteristics of these fine particles; thus, interactions between these particles and the surrounding discontinuous airflow are not taken into account.

The computation of normal forces for particles relies on the Hertzian contact theory, while tangential force calculations are founded on the Mindlin–Deresiewicz work. Both types of forces incorporate damping components. The tangential friction force adheres to the Coulomb law of friction model, and rolling friction is executed under the context-independent directional constant torque model. These force calculations are all consolidated within the Hertz–Mindlin (no slip) physics module of the EDEM software.

For particles with small size, van der Waals forces become significant and they tend to stich to each other. The calculation of the normal force, whether between particle–particle or particle–geometry interactions, differs from that in the Hertz–Mindlin (no slip) physics module. The JKR model is developed for this kind of adhesive and elastic interactions.

According to the theory of Hertz [23,24], the normal pressure distribution acting over the small circular contact area (shown in Figure 1) of radius a is expressed as:

$$p(r) = p_0\left[1 - \left(\frac{r}{a}\right)^2\right]^{\frac{1}{2}}, \tag{1}$$

where $r(r \in [0, a))$ is the distance from the point to the center point of the contact area, and p_0 is the pressure at the center of the contact area. In Figure 1, the dashed arc contour delineates the shape of the two particles prior to contact, while the solid arc contour depicts their shape following the contact. The maximum radius of the contact surface is denoted as 'a' in Figure 1. The $\alpha_{1,2}$ in Figure 1 are the deformations of the two spheres in the normal direction due to contact, respectively. Additionally, the relative approach of the centroids of the two spheres in the normal direction is defined by:

$$\alpha = \alpha_1 + \alpha_2, \tag{2}$$

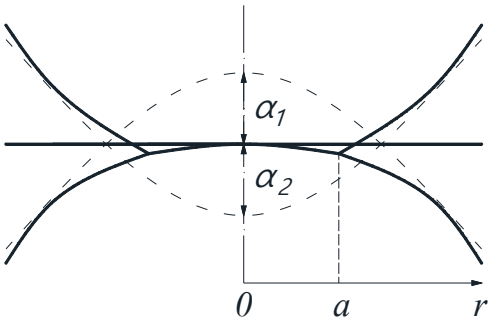


Figure 1. Contact surface between two spheres.

The total normal force is the integral of the pressure on the contact area:

$$F_n = \int_0^a p(r) 2\pi r dr, \tag{3}$$

Considering the van der Waals force, the normal contact pressure distribution is written as [23]:

$$p(r) = p_{def}(r) - p_{van}(r) = \left(\frac{2E^* a}{\pi R^*}\right)\left[1 - \left(\frac{r}{a}\right)^2\right]^{\frac{1}{2}} - \left(\frac{2E^*\Gamma}{\pi a}\right)^{\frac{1}{2}}\left[1 - \left(\frac{r}{a}\right)^2\right]^{-\frac{1}{2}}, \tag{4}$$

where E^* is the relative contact compliance, R^* is the relative curvature of the surface, and Γ is the work of adhesion. The first term of this equation $p_{def}(r)$ signifies the pressure attributed to deformation, while the second term $p_{van}(r)$ corresponds to the pressure induced by the van der Waals force. The formulae for these three variables above are shown in Formulas (5)~(7):

$$E^* = \frac{1}{\frac{1-\nu_1^2}{E_1} + \frac{1-\nu_2^2}{E_2}}, \tag{5}$$

$$R^* = \frac{1}{\frac{1}{R_1} + \frac{1}{R_2}}, \tag{6}$$

$$\Gamma = \gamma_1 + \gamma_2 - \gamma_{1,2}, \tag{7}$$

where $E_i(i = 1, 2)$ and $\nu_i(i = 1, 2)$ are the Young's modulus and the Poisson's ratio for the two spheres, respectively, $R_i(i = 1, 2)$ are the radii of the two spheres, $\gamma_i(i = 1, 2)$ are the surface energies of the two solids, and the $\gamma_{1,2}$ is the interface energy.

The normal force is obtained from Equations (3) and (4):

$$F_n = \frac{4E^* a^3}{3R^*} - \left(8\pi\Gamma E^* a^3\right)^{\frac{1}{2}}, \tag{8}$$

The corresponding relative approach is given by:

$$\alpha = \frac{a^2}{R^*} - \left(\frac{2\pi\Gamma a}{E^*}\right)^{1/2}, \tag{9}$$

Equations (8) and (9) show the revised JKR model used to calculate the normal contact force on a sphere particle considering the van der Walls force.

Consider a surface coating with a structure of uniformly distributed cylindrical crystals of equal height [6], as shown in Figure 2: the actual contact area between a particle and the coating corresponds to the base areas of these cylinders. For a circular region with a radius of R^c, whose area is $A^c = \pi {R^c}^2$, the surface area of the top of the crystal is described as:

$$A^{cr} = n\pi {r^{cr}}^2, \tag{10}$$

where r^{cr} is the radius of the base of the cylinder, and n is the number of the crystals in this region.

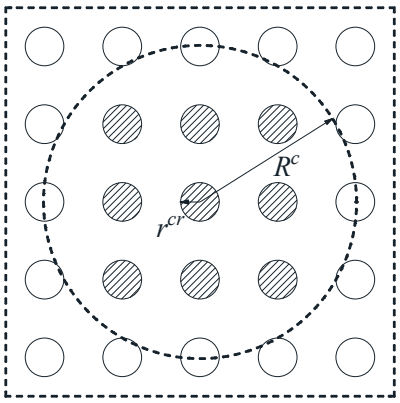


Figure 2. Schematic diagram of coated surface.

The aim of using this particular coating structure is to minimize the actual contact area between the particles and the coating surface, thus reducing the influence of van der Waals forces. When a spherical particle comes into contact with this surface, the actual contact area comprises the combined areas of multiple crystal bottoms, as depicted in

Figure 3. Assuming a uniform variation in pressure from the center of the circle along the radius during this kind of contact, we simplify the reduction of contact area as a decrease in pressure along the radial direction to facilitate calculations. As such, the pressure distribution of the spherical particle on the coating surface can be approximately expressed in the following form:

$$p^c(r) = p^c_{def}(r) - p^c_{van}(r) = \left(\frac{2E^*a^c}{\pi R^*}\right)\left[1-\left(\frac{r}{a^c}\right)^2\right]^{\frac{1}{2}} - \left(\frac{2E^*\Gamma^c}{\pi a^c}\right)^{\frac{1}{2}}\left[1-\left(\frac{n^{\frac{1}{2}}\frac{r^{cr}}{R^c}r}{a^c}\right)^2\right]^{-\frac{1}{2}}, \tag{11}$$

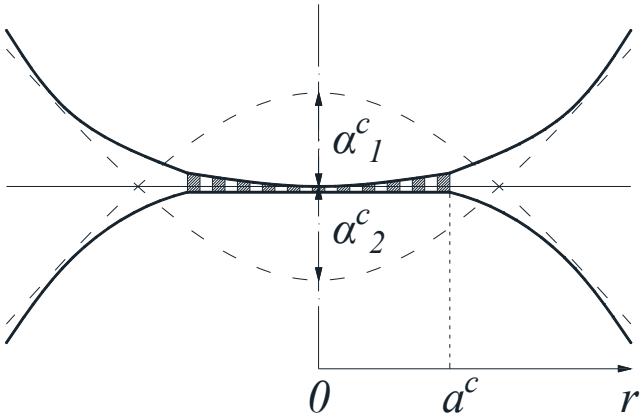


Figure 3. Schematic diagram of particle contact with coated surface.

Analogous to Equation (4), the two terms in Equation (11) denote pressure induced by deformation and the van der Waals force, respectively. However, it is crucial to note that the work of adhesion Γ^c in Equation (11) does not equate to Γ in Equation (4), as the actual contact area diminishes the adhesive effect.

Define a parameter of equivalent area ratio for the coating to describe the ratio of the actual contact area to the projected area of the contact surface:

$$k = \frac{A^{cr}}{A^c} = n\left(\frac{r^{cr}}{R^c}\right)^2, 0 < k \leq 1, \tag{12}$$

Then, Equation (11) can be reformulated as the follow equation:

$$p^c(r) = p^c_{def}(r) - p^c_{van}(r) = \left(\frac{2E^*a^c}{\pi R^*}\right)\left[1-\left(\frac{r}{a^c}\right)^2\right]^{\frac{1}{2}} - \left(\frac{2E^*\Gamma^c}{\pi a^c}\right)^{\frac{1}{2}}\left[1-\left(\frac{k^{\frac{1}{2}}r}{a^c}\right)^2\right]^{-\frac{1}{2}}, \tag{13}$$

Hence, by integrating the pressure over the contact area, we derive the applied normal contact force taking into account the coating:

$$F^c_n = \int_0^{a^c} p^c_{def}(r)2\pi r dr - \int_0^{a^c} p^c_{van}(r)2\pi r dr \quad = \frac{4E^*a^{c3}}{3R^*} - \frac{\left(1-(1-k)^{1/2}\right)}{k}\left(8\pi\Gamma E^*a^{c3}\right)^{1/2}, \tag{14}$$

Similarly, the corresponding relative approach is:

$$\alpha^c = \alpha^1_c + \alpha^2_c = \frac{a^{c2}}{R^*} - \left(\frac{2\pi\Gamma^c a^c}{E^*}\right)^{1/2}, \tag{15}$$

Equations (14) and (15) are used to calculate the normal force of a spherical particle when contacting a surface with a coating.

This model presupposes that the interaction between the particle and the coating does not alter the deformation characteristics of the contact surface, and that the distribution of pressure resulting from the deformation varies uniformly across the contact surface. The

normal forces derived from the solution of this computational model serve as inputs for subsequent computations. These further calculations determine the damping components, along with forces such as tangential and frictional forces.

While performing the DEM simulation, the following iterative calculation steps are adopted:

(1) Compute the positions of the particles and geometry at the current time step;
(2) Based on the position data of each unit, determine the relative approach between particle-to-particle or particle-to-geometry interactions;
(3) Use the relative approach to calculate the normal force exerted on the particles, utilizing the contact model proposed in this paper;
(4) Compute the other forces acting on the particles based on the revised normal force;
(5) Update the motion and position of the particles according to these calculated forces;
(6) Repeat step one until the iteration process reaches completion.

Leverage the API tool to transform the model described above into a plug-in, facilitating its invocation within the EDEM software.

3. Simulations and Discussions

To demonstrate the model presented in this paper, simulations of spherical particles dumping on smooth and coated plates were carried out respectively, based on the Altair EDEM^{TM} 2022.1 software. It is worth noting that we selected the ideal sphere as the physical model for our simulation, primarily to ease the execution of theoretical analysis. While irregular particles might offer a more realistic simulation, analyzing the force and motion of an ideal sphere is considerably more convenient and straightforward, thereby simplifying the derivation of universal laws. Consequently, we opted for the ideal sphere as our physical model to augment our capability to analyze the impact of the two surfaces on fine particles.

3.1. Particles Rolling on a Smooth Plate

Three kind of bulk materials, SiO_2, Fe_2O_3, Fe_3O_4, were created to characterize the motion of different types of particles on a surface. The primary motivation for choosing these materials was their prevalence on the Martian surface, where silicon oxides and iron oxides are among the most commonly found constituents. The reason for selecting two different types of iron oxide materials was to compare the differences that may arise between these two iron oxide particulates during simulated rolling. For comparative data analysis, all particles were designed as ideal spheres. The size distribution was set to follow a standard normal distribution with a mean value of 60 μm and a standard deviation of 0.4. The particle size range was between 10 μm and 110 μm. Each particle consisted of grid cells arranged in a $30 \times 30 \times 30$ ($X \times Y \times Z$) configuration. The plate material was chosen to be SiO_2. Indeed, the protective materials used on the surface of solar panels were meticulously designed to endure the harsh conditions of a Mars exploration mission. However, in the context of this study, our primary focus was on the normalization of the plate relative to fine particles. As such, we opted for silica as the plate material, due primarily to its readily available and well-documented material properties. Three types of particles were deposited onto the horizontal plane via particle factories, with each type represented by 10 particles. After the particles had been dispensed and their relative motion had ceased, the plate was rotated along the y-axis at a constant speed until the particles rolled off the plate. The base contact model used was Hertz–Mindlin with JKR V2, and the friction model employed was standard rolling friction. Gravity was set at 3.71 m/s^2.

To maintain numerical stability and precision throughout the particle dynamics simulation, the time step was configured to be 40% of the Riley time step, equating to 8.74×10^{-10} s. This was determined by taking into account the recommended setting (20~40%) of the EDEM software as well as the iteration speed. Moreover, given that the physical models discussed in this paper did not encompass any additional elements (such as bonds), there was no explicit necessity to shorten the iteration step with the aim of

enhancing simulation stability and precision. The cell size was determined to be 2.5 times the minimum particle radius (R_{min}). While the EDEM's recommended setting for cell size typically ranged from 3 to 6 times the R_{min}, we took into account the diminutive particle size of our physical model in this study. To guarantee solution accuracy, we adjusted the cell size to be set at 2.5 times the R_{min}. Considering the storage space and the continuity of data changes, the time interval for data saving was set to 0.005 s.

The simulation results are shown in Figure 4. Each subplot in Figure 4 depicts a unique time node in the movement of these particles, marking critical instances such as the onset or conclusion of motion.

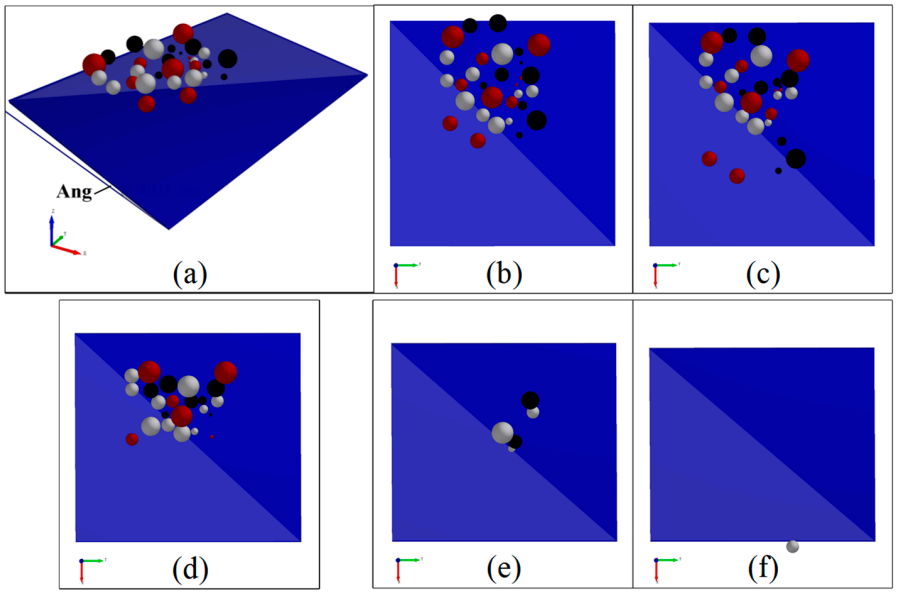


Figure 4. Particle distribution on the plate. Gray: SiO_2, brown: Fe_2O_3, black: Fe_3O_4. (**a**) Diagram of the variable *Ang*; (**b**) *Ang* = 0°; (**c**) *Ang* = 7.00°; (**d**) *Ang* = 22.30°; (**e**) *Ang* = 28.30°; (**f**) *Ang* = 30.70°.

We introduced the variable *Ang* to denote the angle between the smooth plate and the horizontal plane, as depicted in Figure 4a. Initially, the plate was maintained in a horizontal position and particles of the three materials were randomly spread on the plate, as illustrated in Figure 4b. As the rotation of the plate commences, the particles tended to roll off. When *Ang* = 7°, a portion of the particles initiated rolling, except for the SiO_2 particles which remained relatively stationary, showcased in Figure 4c. At the point when *Ang* reached 22.3°, the SiO_2 particles started skidding along with other particles, portrayed in Figure 4d. Yet, some SiO_2 particles persisted on the plate, providing support for Fe_3O_4 particles and preventing them from rolling off. When *Ang* = 28.3°, all residual particles began their roll off the plate, as captured in Figure 4e. Finally, an SiO_2 particle located comparatively near the top also rolled off the plate, as demonstrated in Figure 4f.

In order to illustrate the interactions of van der Waals forces between the particles and the plate, the five particles depicted in Figure 4e are numerically labeled as shown in Figure 5.

The details of these particles are shown in Table 1.

Table 1. Details of the five particles on the plate.

No.	Material	Diameter (μm)	Mass ($\times 10^{-7}$ g)
1	SiO_2	32.6	0.44
2	SiO_2	56.5	2.28
3	SiO_2	97.4	11.64
4	Fe_3O_4	62.4	6.59
5	Fe_3O_4	80.0	13.90

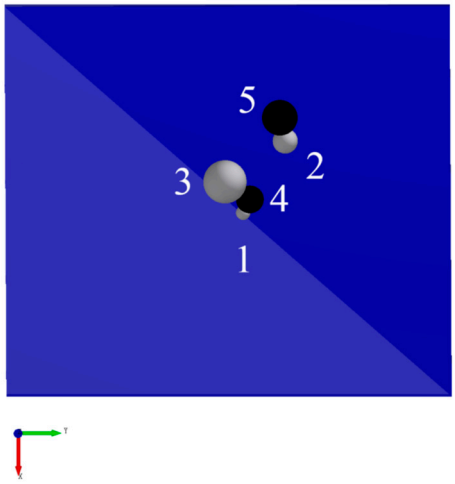


Figure 5. Numbering of particles on the plate. 1, 2 and 3: SiO_2 particles; 4, 5: Fe_3O_4 particles.

Since the mass of different particles varies considerably, define the parameter F_{nm} to describe the normal force per unit mass:

$$F_{nm} = \frac{F_n}{m}, \tag{16}$$

where m represents the mass of a particle.

Utilizing the post-processing tools of EDEM, we obtained the normal force experienced by each particle at each sampling interval. By further dividing these forces by the respective mass of each particle, we derived the changes in F_{nm} over time. Then, extracting the *Ang* value at each sampling interval, we plotted the curves representing the changes in each particle's F_{nm} with respect to variations in *Ang*. The curve representing F_{nm} for angles ranging from *Ang* = 22.7° to *Ang* = 30.7° is plotted in Figure 6. From this figure, it becomes evident that an increase in mass for SiO_2 particles corresponds with a decrease in F_{nm}. In contrast, the slight difference in mass for Fe_3O_4 particles does not result in a significant variation in F_{nm} values. Initially, particle No. 2 supported particle No. 5 as depicted in Figure 4e. However, as these particles rolled off, particle No. 2 was no longer compressed by particle No. 5, resulting in an F_{nm} value approximately around 750 dyn/g.

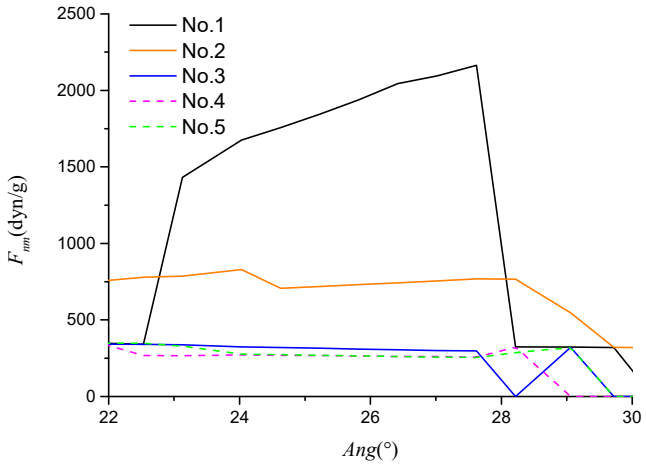


Figure 6. Normal force per unit mass of each particle on the plate.

3.2. Particles Rolling on a Coated Plate

We applied the modified normal force calculation model to the case just discussed, aiming to compute the interaction between particulate matter and the coating. The mi-

crostructure of the coating could not be represented in the EDEM software. Additionally, the EDEM software identifies contact based solely on coordinate distance and ignores surface properties. Hence, we made no additional adjustments for the coating during EDEM processing. In the previous section, we introduced the equivalent area ratio (k) as a parameter to characterize the surface properties of the coating. In this simulation case, we set the value of k in advance for the new plugin to invoke. Setting the equivalent area ratio at $k = 0.5$, we then analyzed the resulting simulation outcomes.

We introduced the normal force model proposed in this study into the EDEM file location as an API plug-in, enabling the calculation of contact forces between particles and a coated plate. We retained the settings from the previous simulation case. The resultant simulation outcomes are represented in Figure 7. Similar to Figure 4, each subplot in Figure 7 also illustrates a distinct time node during the movement of these particles. To clearly denote the coating on the surface of the plate, we depicted the plate in Figure 7 with a color distinct from that in Figure 4, while maintaining the color consistency of particles with those in the preceding simulation case.

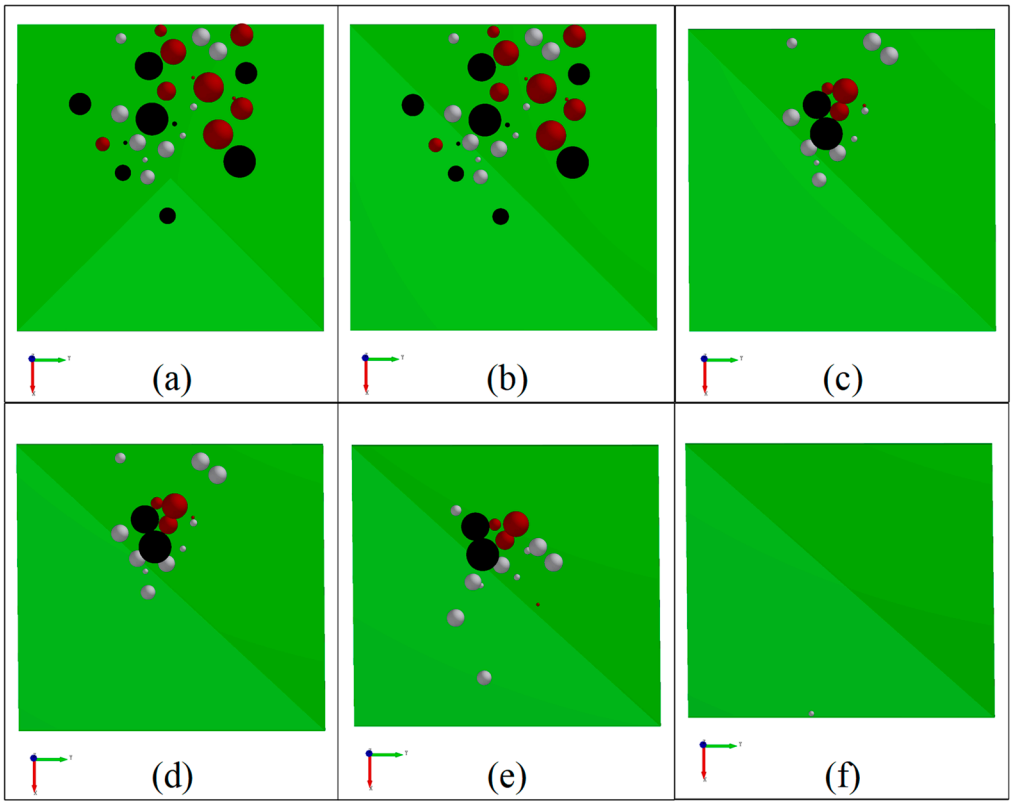


Figure 7. Particle distribution on the coated plate. (**a**) *Ang* = 0°; (**b**) *Ang* = 6.75°; (**c**) *Ang* = 12.40°; (**d**) *Ang* = 23.40°; (**e**) *Ang* = 26.10°; (**f**) *Ang* = 29.30°.

Before the rotation of the plate began, particles of three different materials were randomly dispersed on it, as displayed in Figure 7a. Once these particles settled into a relatively stationary state, the rotation of the plate initiated. When the plate was rotated to *Ang* = 6.75°, certain particles started rolling downward, as portrayed in Figure 7b. The SiO_2 particles remained static, and some Fe_2O_3 and Fe_3O_4 particles ceased their downward roll due to their reliance on the SiO_2 particles, as illustrated in Figure 7c. It was not until the plate was rotated to *Ang* = 23.4° that SiO_2 particles initiated their downward roll, as captured in Figure 7d. Consequently, the Fe_2O_3 and Fe_3O_4 particles commenced their descent due to the loss of support from the SiO_2 particles. All particles collectively rolled down off the plate, as demonstrated in Figure 7e. Eventually, the smallest SiO_2 particle became the last one to roll off the plate, as shown in Figure 7f.

Analogously, a few representative particles found in Figure 7d were selected and numerically labeled as demonstrated in Figure 8. Numbers 6 and 7 refer to two SiO_2 particles, one interacting with other particles and the other solely making contact with the plate's coating. Number 8 represents a Fe_2O_3 particle, and number 9 denotes a Fe_3O_4 particle.

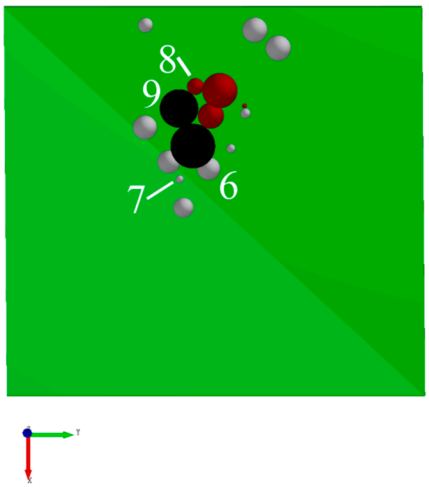


Figure 8. Numbering of particles on the coated plate.

The details of these particles are shown in Table 2.

Table 2. Details of the four particles on the coated plate.

No.	Material	Diameter (μm)	Mass ($\times 10^{-7}$ g)
6	SiO_2	55.8	2.19
7	SiO_2	18.7	0.08
8	Fe_2O_3	39.8	1.73
9	Fe_3O_4	92.0	21.11

The variations in the normal force per unit mass of these particles are depicted in Figure 9. Given that particle No. 6 supported several particles above it, it experienced substantial pressure, thereby resulting in a high F_{nm} value. For particles No. 7 and No. 8, their F_{nm} values were roughly similar. It is plausible that the smaller mass of particle No. 7 led to it having a slightly larger F_{nm} value than that of particle No. 8. Despite having the largest mass, particle No. 9 exhibited the smallest F_{nm} value compared to the others. The mass of particle No. 6 was akin to that of particle No. 2. Upon comparing Figures 6 and 9, it is evident that the F_{nm} value of particle No. 6 exceeded that of particle No. 2 during the downward rolling progress. This discrepancy can likely be attributed to the coating's mitigation effect on van der Waals forces.

Particle No. 3 in Figure 6 and particle No. 7 in Figure 9, both composed of the same material, remained intact during the rolling down process. The F_{nm} values for these two particles were close to each other, but the value of particle No. 7 (~330 dyn/g) was marginally higher than that of particle No. 3 (~300 dyn/g) throughout the rolling process. In addition, upon comparing Figures 4c and 7b, it becomes evident that the initiation angle of the particles diminished from 7.00° to 6.75°, a change attributable to the presence of the coating. Consequently, it is markedly evident that the presence of the coating increased the normal force exerted on the fine particles, thereby facilitating the ease with which particles rolled off the plate. Nevertheless, as observed from particle No. 1 in Figure 4 and particle No. 6 in Figure 7, irrespective of the coating's presence or absence, some particles remained adhered to the plate surface, consequently preventing other particles from rolling off the plate. Moreover, there were differences in the adsorption of particles composed

of diverse materials on the plate. As can be seen in both Figures 4 and 7, SiO_2 spherical particles appeared to adhere more readily to the SiO_2 plate compared to their iron oxide counterparts. This phenomenon could potentially be attributed to the inherent material properties of the particles or the interactive properties exhibited during its contact with the plate.

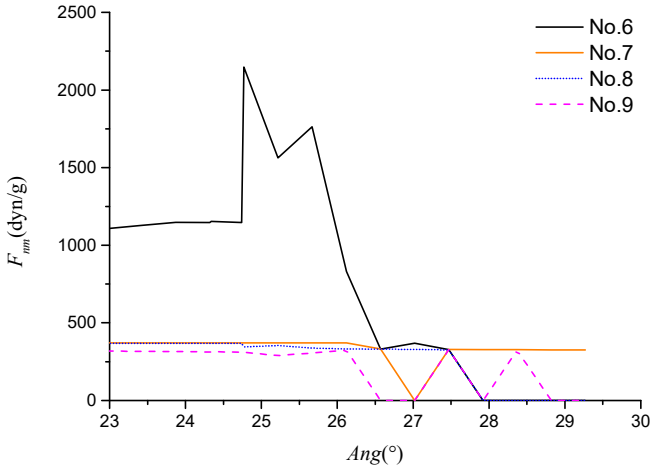


Figure 9. Normal force per unit mass of each particle on the coated plate.

Based on the above simulation cases, we can find that:

- The adherence of minuscule particles to the plate acted as a barrier, preventing larger particles from rolling off the plate;
- The presence of the coating weakened the van der Waals force, resulting in an increase in the normal force;
- Owing to the impact of the coating, tilting the plate facilitated easier rolling off of particles.

It is important to note that the primary objective of this study was to propose a novel computational model and associated method for researchers to investigate the dust removal capabilities of coatings. Consequently, our focus lay in assessing the feasibility of this method by analyzing particle force and motion. To facilitate the analysis, we established an ideal sphere model for the rolling simulation, while not performing simulations with plates tilted at 90°, as compared to common tilting tests. Furthermore, factors such as air humidity, particle shape, and surface roughness greatly influenced particle adhesion to the plate. The numerical simulation of large quantities of fine particles tilting proved to be both time-consuming and complex. Therefore, this research did not undertake comprehensive particle dumping simulations for comparison with relevant experiments. Future research can explore the effects of particle shape on adsorption properties by introducing irregularly shaped particles into the dump.

4. Conclusions

This paper addresses the issue of fine particulate adsorption on solar panels in Mars's environment. A model was developed to calculate the contact force between the fine particles and the coated surface, utilizing an approximate equivalent pressure measure. We executed the motion simulation of fine particles through the API module of EDEM software. By simulating the movements of particles on a smooth plate and a coated plate, we compared the differences in solution results between the JKRV2 model and our proposed model.

The outcomes of our simulation underscore that the adherence of minuscule particles to a plate acts as a deterrent, impeding other particles from rolling off. The coating attenuates the adsorption of particles, but does not completely eliminate the adsorption of particles.

Future work will concentrate on exploring the agglomeration effects of particles and studying the adsorption of complex-shaped particles on plates.

Author Contributions: Conceptualization, H.W. and M.L.; methodology, H.W. and M.L.; software, H.W.; validation, H.W. and M.L.; formal analysis, M.L.; investigation, H.W.; resources, H.W.; data curation, H.W.; writing—original draft preparation, H.W.; writing—review and editing, H.W. and M.L.; visualization, H.W.; supervision, M.L.; project administration, M.L. All authors have read and agreed to the published version of the manuscript.

Funding: This research received no external funding.

Institutional Review Board Statement: Not applicable.

Informed Consent Statement: Not applicable.

Data Availability Statement: The datasets presented in this article are not readily available because the data are part of an ongoing study or due to technical limitations. Requests to access the datasets should be directed to the corresponding author.

Conflicts of Interest: The authors declare no conflicts of interest.

References

1. Lorenz, R.D.; Martinez, G.M.; Spiga, A.; Vicente-Retortillo, A.; Newman, C.E.; Murdoch, N.; Forget, F.; Millour, E.; Pierron, T. Lander and rover histories of dust accumulation on and removal from solar arrays on Mars. *Planet Space Sci.* **2021**, *207*, 105337. [CrossRef]
2. Callas, J.L.; Golombek, M.P.; Fraeman, A.A. *Mars Exploration Rover Opportunity End of Mission Report*; Jet Propulsion Laboratory, National Aeronautics and Space Association: Pasadena, CA, USA, 2019.
3. Bowman, A. NASA Retires InSight Mars Lander Mission After Years of Science. Available online: https://www.nasa.gov/missions/insight/nasa-retires-insight-mars-lander-mission-after-years-of-science/ (accessed on 5 February 2024).
4. Waldek, S. NASA's Mars Reconnaissance Orbiter Confirms that China's Zhurong Rover Has Been Stationary for Months. Available online: https://www.space.com/mars-reconaissance-orbiter-zhurong-rover-images (accessed on 5 February 2024).
5. Landis, G.A. Mars dust removal technology. In Proceedings of the IECEC-97 Proceedings of the Thirty-Second Intersociety Energy Conversion Engineering Conference (Cat. No.97CH6203), Honolulu, HI, USA, 27 July–1 August 1997.
6. Xu, Y.; Wi, Z.; Wang, Z.; Tian, D. Exploration for Nano-crystalline Composite Coatings in Dust-proof of Cover Glasses on Mars. *Surf. Technol.* **2019**, *48*, 167–171. (In Chinese)
7. Good, A.; Fox, K.; Johnson, A. NASA's InSight Mars Lander Gets a Power Boost. Available online: https://www.nasa.gov/centers-and-facilities/jpl/nasas-insight-mars-lander-gets-a-power-boost/ (accessed on 5 February 2024).
8. Calle, C.I.; Buhler, C.R.; Johansen, M.R.; Hogue, M.D.; Snyder, S.J. Active dust control and mitigation technology for lunar and Martian exploration. *Acta Astronaut.* **2011**, *69*, 1082–1088. [CrossRef]
9. Zhang, J.W.; Wang, W.Q.; Zhou, S.X.; Yang, H.D.; Chen, C. Transparent dust removal coatings for solar cell on mars and its Anti-dust mechanism. *Prog. Org. Coat.* **2019**, *134*, 312–322. [CrossRef]
10. Tian, H.; Zhang, T.; Jia, Y.; Peng, S.; Yan, C. Zhurong: Features and mission of China's first Mars rover. *Innov.-Amst.* **2021**, *2*, 100121. [CrossRef] [PubMed]
11. Zhang, J.W.; Zhou, S.X. Preparation and properties of anti-dust coatings for the photovoltaic cell of Martian rover. *J. Fudan Univ. (Nat. Sci.)* **2019**, *58*, 740–746.
12. Dogra, V.; Kishore, C.; Mishra, A.; Gaur, A.; Verma, A. Sol-Gel preparation and wetting behaviour analysis of hydrophobic Zirconium based nano-coating: Implications for solar panel coating. *Chem. Eng. J. Adv.* **2023**, *15*, 100507. [CrossRef]
13. Perko, H.A.; Nelson, J.D.; Green, J.R. Review of martian dust composition, transport, deposition, adhesion, and removal. In Proceedings of the Space 2002 and Robotics 2002, Albuquerque, NM, USA, 17 March 2002; pp. 176–189.
14. Kok, J.F.; Parteli, E.; Michaels, T.I.; Karam, D.B. The physics of wind-blown sand and dust. *Rep. Prog. Phys.* **2012**, *75*, 106901. [CrossRef] [PubMed]
15. Coetzee, C.E.J. Calibration of the discrete element method. *Powder Technol.* **2017**, *310*, 104–142. [CrossRef]
16. Kruggel-Emden, H.; Rickelt, S.; Wirtz, S.; Scherer, V. A study on the validity of the multi-sphere Discrete Element Method. *Powder Technol.* **2008**, *188*, 153–165. [CrossRef]
17. Huang, P.P.; Xiao, X.Z. Simulation study the movement of materials in loader shovel working process based on EDEM. *Adv. Mater. Res.* **2013**, *655*, 320–325. [CrossRef]
18. Song, G.; Huang, F.; Pan, J. Feasibility Analysis of Calcium Carbonate Particle Trajectory Simulation in a Dual Horizontal Shaft Mixer. *Materials* **2023**, *16*, 5999. [CrossRef] [PubMed]
19. Barrios, G.K.; Jimenez-Herrera, N.; Fuentes-Torres, S.N.; Tavares, L.M. DEM Simulation of Laboratory-Scale Jaw Crushing of a Gold-Bearing Ore Using a Particle Replacement Model. *Minerals* **2020**, *10*, 717. [CrossRef]

20. Johnson, K.L.; Kendall, K.; Roberts, A. Surface energy and the contact of elastic solids. *Proc. R. Soc. London. A. Math. Phys. Sci.* **1971**, *324*, 301–313.
21. Altair Engineering Inc. Coupling Interface Programming Guide. Available online: https://2022.help.altair.com/2022.1/EDEM/Coupling_Interface_Programming_Guide.htm (accessed on 5 February 2024).
22. Bird, G.A. *Molecular Gas Dynamics and the Direct Simulation of Gas Flows*; Oxford University Press: Oxford, UK, 1994.
23. Johnson, K.L. *Contact Mechanics*; Cambridge University Press: Cambridge, UK, 1985.
24. Thornton, C. *Granular Dynamics, Contact Mechanics and Particle System Simulations: A DEM Study*, 1st ed.; Springer International Publishing: Berlin/Heidelberg, Germany, 2015.

Disclaimer/Publisher's Note: The statements, opinions and data contained in all publications are solely those of the individual author(s) and contributor(s) and not of MDPI and/or the editor(s). MDPI and/or the editor(s) disclaim responsibility for any injury to people or property resulting from any ideas, methods, instructions or products referred to in the content.